Modelling inland Arctic bathymetry from space using cloud-based machine learning and Sentinel-2

Michael A. Merchant

Ducks Unlimited Canada, 10525 170 Street, Suite 300, Edmonton, Alberta T5P 4W2, Canada

Abstract

Lakes and ponds are extensive features throughout the circumpolar region, spanning a broad range of environmental conditions which controls their hydro-ecological processes and spatiotemporal distribution. The physical characteristics of these freshwater ecosystems, including their extent and depth, are particularly responsive to climatic conditions. Thus, having the ability to efficiently map and monitor these elements is crucial as the climate continues to warm, especially over large spatial extents. In this study, satellite derived bathymetry (SDB) methods were implemented to model regional inland Arctic water depths within the open-source and cloud-based Google Earth Engine (GEE) platform. High-resolution (10 m) spectral reflectance data from Sentinel-2 was used as covariates in non-parametric and non-linear machine learning (ML) models, namely random forest (RF), support vector regression (SVR), and classification and regression trees (CART). These three ML models were also compared to a more classical and parametric multiple linear regression (MLR) model. All models were calibrated using in situ bathymetric data collected near the Toolik Field Station, in the Alaskan Arctic tundra. With such a large sample repository available, the effects of training set size, noise, and multicollinearity on model performance was comprehensively investigated. Results clearly demonstrated the superior efficacy and robustness of the RF algorithm for predicting water depths, achieving a best coefficient of determination (R^2) of 0.74, mean absolute error (MAE) of 2.12 m, and root mean square error (RMSE) of 3.04 m. Overall, this study highlights the potential of advanced and flexible ML algorithms within the GEE, and demonstrates the capabilities of the polar-orbiting Copernicus Sentinel-2 satellite for this Arctic application. In the future, this ML-driven methodology can be applied using GEE's cloud infrastructure to produce updated, cost-effective, and accurate bathymetry maps over large expanses of the Arctic tundra.

© 2023 COSPAR. Published by Elsevier B.V. All rights reserved.

Keywords: Arctic; Bathymetry; Google Earth Engine; Machine Learning; Sentinel-2

1. Introduction

Tens of thousands of lakes and ponds exist in the continuous permafrost region of the Arctic tundra (Paltan et al., 2015). These are significant freshwater ecosystems that influence a multitude of hydrological, ecological, and biogeochemical processes, such as evapotranspiration, groundwater fluctuations, and carbon storage and cycling, to name a few (Bring et al., 2016). At high latitudes, many of these waterbodies develop from thermokarst erosional processes, in which permafrost is degraded when water begins to pool in the summer causing reduced surface albedo and localized warming (Hinkel et al., 2012; Hopkins, 1949). Recent studies have shown that lakes and wetlands are rapidly changing (e.g., shrinking and/or expanding) in some regions of the Arctic (Jepsen et al., 2013; Riordan et al., 2006), a result of their sensitivity to climatic conditions (Vincent et al., 2013). Given that the arctic is experiencing precipitous warming (i.e., a phenomenon referred to as "polar amplification"; Manabe &

E-mail address: m_merchant@ducks.ca

Stouffer, 1980), this represents substantial potential for further shifts in waterbody conditions, including extent and depth, from permafrost-related drivers (Plug & West, 2009; Rautio et al., 2011). Hence, the mapping and monitoring of Arctic waterbodies is a crucial task. While numerous studies have previously demonstrated the accurate mapping of inland Arctic surface water extent and abundance from space (Carroll & Loboda, 2017; Cooley et al., 2019; Muster et al., 2013; Sui et al., 2018), less so have established methods capable of retrieving bathymetry, especially at regional scales and/or high-resolution. As such, there is a need for timely and accurate maps that depict bathymetric information over broad extents of the Artic.

Bathymetry has conventionally been mapped using either labor-intensive field surveys, or acoustic echo sounding technologies (e.g., sonar) aboard vessels (Gao, 2009). The former often lacks desired accuracy (Liu et al., 2003), whereas the later, while relatively advanced and accurate, are problematic in shallow waters (<3 m), costly, and impractical over large spatial extents (Richards & Leighton, 2003). The impracticality of such methods is further compounded by the remoteness and often inaccessibility of regions like the high-arctic. An alternative technique to retrieving bathymetry is by exploiting the spectral information collected from passive optical data, including multi- and hyper-spectral sensing technologies. Methods to do so were first investigated in the 1970 s by Polcyn et al. (1970), whereby water depth was determined by measuring wave refraction changes and the Fourier transform plane. Since then, a vast number of studies have demonstrated the efficacy of depth retrieval using optical sensors aboard satellite platforms (e.g., Landsat, Sentinel-2, etc.), especially in marine and coastal environments (Caballero & Stumpf, 2019; Hedley et al., 2018; Poursanidis et al., 2019; Yunus et al., 2019). These techniques are commonly referred to as Satellite Derived Bathymetry (SDB) in the literature.

Retrieving bathymetric information with a remote sensor relies on the radiative transmission principle in which the total amount of upwelling radiation energy (L_t) reflected from a water column is a function of depth (Gao, 2009; Fig. 1). This is explained according to Beer's Law, in which light decreases exponentially in water as the depth increases (Lyzenga, 1978). Furthermore, the L_t recorded by a passive optical sensor over a waterbody is the sum of four main components:

$$L_t = L_p + L_s + L_v + L_b \qquad (1)$$

where L_p is 'atmospheric path radiance' energy resulting from sun radiation that does not reach the water surface; L_s is energy that arrives at the air–water interface, enters a short depth (e.g., a millimeter) into the water column, and then is reflected back to the sensor; L_v is 'subsurface volumetric radiance' that is reflected after further penetrating the water column and interacting with constituents (e.g., chlorophyll, sediments, or dissolved organic matter); L_b is energy that interacts with the water bottom, giving
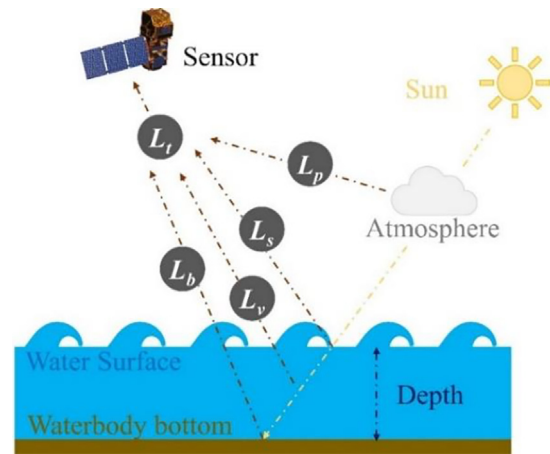

Fig. 1. Radiative transfer process for total radiance (L_t) measured by an optical satellite sensor over a waterbody, whereby l_b is related to water depth (i.e., bathymetry).

bathymetric depth information (Bukata et al., 2018; Campbell & Wynne, 2011; Legleiter & Roberts, 2005; Shah et al., 2020). Thus, retrieving bathymetric depth (i.e., L_b) from an imaging sensor requires the signal contributions of L_v, L_p, and L_s to be adjusted in the equation, resulting in the following:

$$L_b = L_t (L_v + L_p + L_s) \qquad (2)$$

However, accurately quantifying each component in this equation can be challenging due to several practical issues, such as the need for adequate water clarity, homogeneity in bottom type, and optimal atmospheric conditions. In practice, these circumstances seldom occur. Also, the amount of water-leaving radiation is often lesser compared to other sources (e.g., the atmosphere, the water surface, etc.), emphasizing the need for precise atmospheric correction (Ilori & Knudby, 2020).

There are two primary approaches for quantifying (i.e., extracting) L_b using optical remote sensing: physics-based methods and empirical methods (Ashphaq et al., 2021; Gao, 2009). Physics-based inversion approaches rely on modelling the radiative transfer processes of different media. These methods eliminate the need for a-priori depth data, although they are complex and computationally expensive. In contrast, empirical methods rely on in situ bathymetric measurements to model a regression. Among empirical approaches, the two most applied algorithms are the log-linear Lzyenga model (Lyzenga, 1978) and the band-ratio Stumpf model (Stumpf et al., 2003). Although, more recently, optimization-driven machine learning (ML) methods have become a popular approach in bathymetric research. ML algorithms have proven advantageous in this field because of their ability to automatically investigate multi-dimensional remote sensing features and water depth in variable environments (Dickens & Armstrong, 2019; Eugenio et al., 2022; Gafoor et al., 2022; Hassan & Nadaoka, 2017; Manessa et al., 2016; Misra et al., 2018; Mudiyanselage et al., 2022; Sagawa et al., 2019; Surisetty

et al., 2021; Tonion et al., 2020; Yang et al., 2022; Zhang et al., 2019). Hence, ML algorithms can account for diverse and non-linear environmental conditions caused by a range of phenomena, such as turbidity and bottom materials (Ashphaq et al., 2022).

Despite the advancements made in bathymetric modelling from space, literature on such applications over the Arctic is sparse. This is especially the case over onshore areas (e.g., inland lakes and ponds), as most efforts at high latitudes have focused on offshore navigable waters like coastal areas and oceans (Ahola et al., 2018; Chénier et al., 2018; Pe'eri et al., 2016; Zhang et al., 2019). Moreover, the few previous onshore domain studies are limited in their scalability (e.g., desktop-based modelling; Legleiter et al., 2014), resolution (e.g., 30 m Landsat-8; Chen et al., 2022; Simpson et al., 2021), or repeatability due to the deployment of expensive remote sensing technologies (e.g., Light Detection and Ranging; Saylam et al., 2017).

The objective of this study is to address the collective shortcomings of SDB over inland Arctic waterbodies by utilizing ML methods exclusively within the cloud-based Google Earth Engine (GEE) platform. GEE's cloud infrastructure was selected for this study because of its ability to perform efficient, large-scale, and on the fly preprocessing, processing, and analysis (Li et al., 2021; Traganos et al., 2018). Moreover, the predictive performance and robustness of several advanced ML algorithms available within the GEE were evaluated over the Upper Central Brooks Foothills region, Alaska. The ML-based approach estimated the bathymetric depth of 6282 Arctic waterbodies using high-resolution spectral reflectance data from the European Space Agencies (ESA) Copernicus Sentinel-2A and −2B satellites. As such, this study seeks to support the large-scale, efficient, and robust mapping of Arctic biome bathymetry using spaceborne and cloud-based technologies.

2. Materials and methods

2.1. Study area

The selected study area was the Upper Central Brooks Foothills region, Alaska (Muller et al., 2018; Fig. 2). This 33,565 km^2 area, located on the northern flank of the Brooks Range, is home to the Toolik Field Station (TFS; 68°38′ N, 149°36′W). TFS is an ecological research station operated by the University of Alaska Fairbanks with a long history of scientific measurements dating back to 1975 (Selimovic et al., 2022). This area is underlaid by thick, continuous permafrost (200 – 600 m) which has impeded drainage, promoted the saturation of soils, and made thermokarst features very common. Moreover, according to Hinkel et al. (2012), many of the lakes in this region have formed from these thermokarst processes

within aeolian sand deposits. The area also has several deposits left by major Cenozoic glaciations (Ellis & Calkin, 1979), which have influenced water chemistry and vegetation. The latter includes common tundra vegetation types, such as tussock-forming sedges, dwarf shrubs, and mosses (Walker et al., 2005).

2.2. In situ depth measurements

Bathymetric data was surveyed by Stuckey et al. (2019) and acquired from the National Science Foundation's (NSF) Arctic Data Center. The data set is openly published and available from the NSF data portal (https://arcticdata.io/catalog/data). Bathymetric measurements were collected in situ with a Seafloor Sonarmite Hydrolite-TM Echosounder in conjunction with a Trimble GeoExplorer 6000XH global navigation satellite system (GNSS) receiver. The receiver had a Zephyr 2 antennae. Depth measurements were post processed by Stuckey et al. (2019) using Trimble GPS Pathfinder Office. Measurements had a reported vertical accuracy of ± 0.01 m/0.1 percent of depth and a horizonal accuracy of ± 0.5 m.

Once downloaded, the in-situ data required cleaning by removing all measurements with a value of 0, as these corresponded to anomalous, non-water measurements at the margins of waterbodies. Measurements then needed to be resampled to include only one point per Sentinel-2 pixel. This was done by averaging all intersecting depth measurements within a given 10 m pixel. The final processed data set included 31,388 depth measurements (Table 1). Given the large size of the data set, samples were randomly split 50–50% into training and testing.

2.3. Google Earth Engine

Bathymetric modelling of the Upper Central Brooks Foothills region was implemented using GEE (Gorelick et al., 2017; Pérez-Cutillas et al., 2023). GEE is a high-performance, cloud-based geospatial platform that offers global-scale analysis capabilities and access to a multi-petabyte catalog of satellite imagery. Over 40 years of Earth observation (EO) imagery is included in this catalog, including data sets from the well-known Landsat program, Moderate Resolution Imaging Spectroradiometer (MODIS), and the Copernicus Sentinel-1, −2, and −3 missions. By leveraging Google's cloud infrastructure, GEE enables parallel processing of geospatial data at unprecedented computational speeds and scales. This makes GEE an ideal platform for solving geospatial big data problems, such as mapping at ecoregion scales. By being cloud-based, GEE removes user dependency on desktop storage and processing, as well as costly commercial software. All image collection, image preprocessing, and algorithm development was completed using GEE's Javascript code editor Application Programming Interface (API).
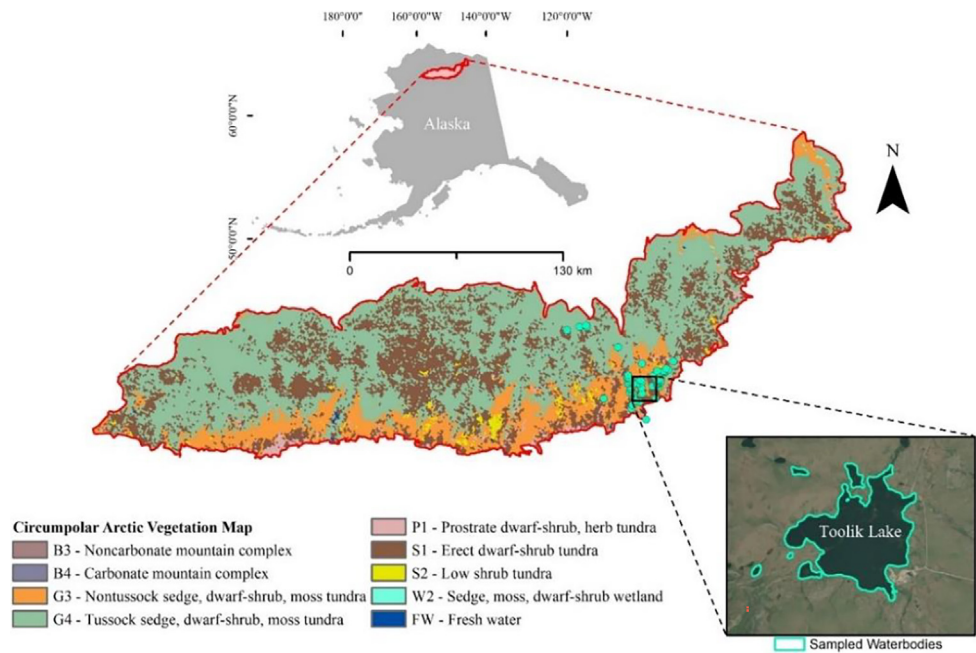
Fig. 2. Study area map. The red area represents the Upper Central Brooks Foothills region. The general vegetation classes are from Walker et al. (2005). Waterbodies sampled for bathymetry are displayed in teal.

Table 1
Descriptive statistics for the bathymetric measurements used in this study.

Samples	Count	Waterbody Depth (m)					
		Minimum	Maximum	Range	Std. Deviation	Mean	Median
Training	15,694	0.01	37.34	37.33	5.73	6.24	4.40
Testing	15,694	0.02	37.88	37.85	5.83	6.32	4.50
All	31,388	0.01	37.88	37.86	5.78	6.28	4.45

2.4. Sentinel-2 imagery and preprocessing

There are numerous factors that affect the atmosphere, water surface, and water column which can impede bathymetric mapping using optical satellite imagery. Common examples include cloud cover, sun glint, and turbidity. To address this, a suitable image preprocessing chain was implemented within GEE. First, Sentinel-2 Multispectral Instrument (MSI) Level-2A images (ee.ImageCollection(" COPERNICUS/S2_SR")) were selected from the GEE which have been radiometrically calibrated and atmospherically corrected using the Sen2Cor algorithm (Louis et al., 2016). The outputs of this correction step are Bottom of Atmosphere (BOA) reflectance images. Previous studies have shown that Sen2Cor is an ideal atmospheric correction method for bathymetric applications (Gafoor et al., 2022). Next, the BOA images were further queried by applying a criterion to remove all observations with cloud coverage greater than 20%. The remaining images were cloud masked using the quality assessment (QA60) bitmask and aerosol bands. A 10 m resolution image composite was prepared using the median pixel values of the processed

images, representing the time-period of July-01–2019 to September-30–2019 (i.e., available ice-off images closest in time to the in-situ surveys).

The final preprocessing step involved log transforming each reflectance band from the median composite, which is a common technique that accounts for the exponential decrease in light with depth (Gafoor et al., 2022; Gao, 2009; Muhammad et al., 2020). To demonstrate the effect of this step, the Pearson correlation coefficient (R) was calculated between reflectance bands and measured water depth. As seen in Table 2, all bands showed a higher correlation to water depth after being log transformed. As such, the log transformed bands, in addition to two traditional band ratios (lnB2/lnB3 and lnB2/lnB4), were included in the ML modelling. Band ratios were chosen based on earlier research on the attenuation of electromagnetic radiation, which has demonstrated that shorter wavelengths often better penetrate the water column (Mishra et al., 2005). Thus, blue bands are commonly ratioed with red and/or green bands to maximize the sensitivity to water depth (Casal et al., 2019).

Table 2

Sentinel-2 sensor specifications and the correlation of spectral bands and their log-transform to in situ measured water depth. The difference (Δ) in R is also calculated.

Central Wavelength (μm)	Spatial Resolution (m)	Sentinel-2 Band	R	Log Transformed Band	R	ΔR
0.443	60	B1	−0.46	lnB1	−0.49	0.03
0.490	10	B2	−0.40	lnB2	−0.43	0.03
0.560	10	B3	−0.45	lnB3	−0.48	0.03
0.665	10	B4	−0.49	lnB4	−0.58	0.09
0.705	20	B5	−0.54	lnB5	−0.62	0.08
0.740	20	B6	−0.51	lnB6	−0.61	0.10
0.783	20	B7	−0.52	lnB7	−0.63	0.11
0.842	10	B8	−0.48	lnB8	−0.61	0.13
0.865	20	B8A	−0.52	lnB8A	−0.63	0.11
1.610	20	B11	−0.53	lnB11	−0.65	0.12
2.190	20	B12	−0.53	lnB12	−0.65	0.12

2.5. Machine learning algorithms

Over recent decades, several non-parametric ML algorithms have been developed and applied for regression tasks with remote sensing data (Verrelst et al., 2015). These methods are frequently referred to as machine learning regression algorithms (MLRA). These ML methods are considered to be non-parametric because they do not make assumptions about data distributions (i.e., structure) or variable interrelations (Gautam & Singh, 2020). Unlike simple parametric methods (e.g., Logistic Regression, Linear Discriminant Analysis, or Naïve Bayes, etc.), which assume an explicit relationship between spectral and environmental observations, non-parametric ML methods can effectively incorporate or fit data sets with non-normal distributions, while also exploiting the full spectrum. Thus, non-explicit and non-linear relationships between spectral features and a given observations (e.g., water depth) can effectively be modelled using MLRAs. This holds advantages for modelling complex variables such as bathymetry over a range of environmental conditions (e.g., turbidity, substrate, etc.). In this study, three different MLRAs available within GEE were assessed for bathymetric modelling, including Classification and Regression Trees (CART), Random Forest (RF), and Support Vector Regression (SVR; Fig. 3). These are described in the following sections.

2.5.1. Classification and regression trees

CART was introduced by Breiman (2001) and is considered a Decision Tree (DT) algorithm since it is rule-based (Lawrence & Wright, 2001). CART is a construction of binary trees that partitions data into a particular node using a cut-off value from an independent variable. With this partitioning procedure, data points are clustered as close together within one group and as far as possible from the other group. The CART algorithm cycles through the independent predictor variables looking for optimal cut-offs, which eventually maximizes deviance. Trees are successively grown by applying this method at each node, each with a unique partitioning rule that minimizes relative error. Implementation of CART within GEE was done using the ee.Classifier.smilaCART algorithm. The 'max-Nodes' parameter, which specifies the maximum number of leaf nodes, was set to unlimited, and 'minLeafPopulation, which specifies the minimum pointed needed for a new node, was set to one.

2.5.2. Random Forest

The foundation of the RF algorithm is CART trees. RF is an ensemble ML algorithm that employs many decision tree classifiers (e.g., CART), whereby each tree votes on the final result. In the case of a regression, the final prediction is the average (i.e., rather than the majority for classification). Each decision tree used in the RF is considered a
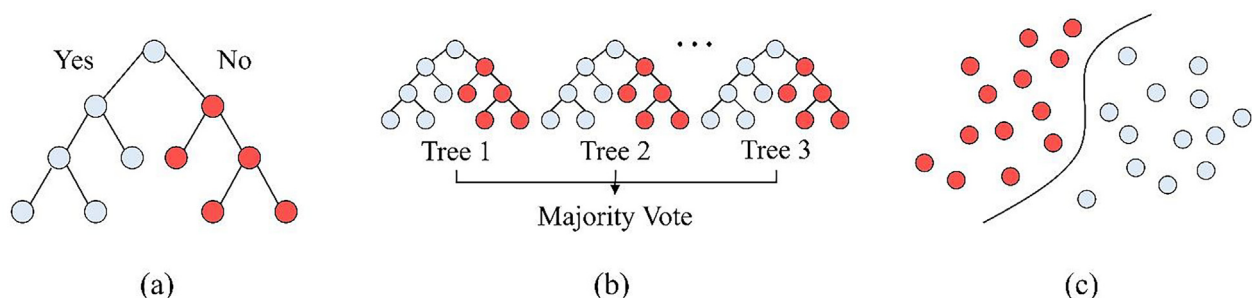

Fig. 3. Schematic representation of ML algorithms assessed in this study. (a) CART. (b) RF. (c) SVR.

weak learner, which when combined in an ensemble (e.g., through voting), produces a stronger RF model. Implementation of RF within GEE was done using the ee.Classifier.smileRandomForest algorithm. Key hyperparameters included 'numberOfTrees', which was set to 300 (i.e., a relatively high number; Amani et al., 2020) and 'variablesPerSplit' (i.e., also known as mtry), which was set to the square root of the number of predictor variables.

2.5.3. Support vector regression

Support vector regression (SVR) employs the same principles as support vector machine (SVM), but for regression (Mountrakis et al., 2011). SVR employs a kernel-based structure and maps data to a high-dimensional space. In doing so, SVR minimizes loss by using a hyperplane that distinctly separates data points. Implementation of SVR within GEE was done using the ee.Classifier.libsvm algorithm and using a radial basis function (RBF) kernel, due to its stability (Guohe, 2011). Other key hyperparameters included 'gamma', which was set to 0.5, and 'cost' which was set to 10 based on trial and error.

2.6. Multiple linear regression

The three non-parametric ML algorithms were also compared to a Multiple Linear Regression (MLR) model, which is commonly used in bathymetric studies (Niroumand-Jadidi et al., 2018). This allowed for the direct comparison of advanced ML algorithms against conventional regression methods. MLR is a regression model that statistically explains the relationship between a dependent variable and multiple independent (i.e., predictor) variables (Maulud & Abdulazeez, 2020). Hence, MLR is the extension of ordinary least-squares (OLS) regression. In this study, bathymetric depth is considered the dependent variable whereas the spectral variables are considered the independent variables (Fig. 3). MLR was implemented within GEE using the ee.Reducer.linearRegression algorithm.

2.7. Model performance evaluations

Model predictions were evaluated using a suite of common validation statistics, including the coefficient of determination (R^2), mean absolute error (MAE), mean squared error (MSE), and root mean square error (RMSE). These were calculated using the following:

$$R^2 = 1 - \frac{\sum (y_i - \widehat{y})^2}{\sum (y_i - \widehat{y})^2} \tag{3}$$

$$MAE = \frac{1}{N} \sum_{i=1}^{N} |y_i - \widehat{y}| \tag{4}$$

$$MSE = \frac{1}{N} \sum_{i=1}^{N} (y_i - \widehat{y})^2 \tag{5}$$

$$RMSE = \sqrt{\frac{1}{N} \sum_{i=1}^{N} (y_i - \widehat{y})^2} \tag{6}$$

where n ($i = 1,2..., n$) is the number of samples used for modelling, y_i is the measured waterbody depth, and $\widehat{y}$ is the predicted depth. R^2 represents the ratio of the variance for the dependent variable that is explained by the independent variables, with values close to 1 indicating high model performance (Plevris et al., 2022). MAE evaluates the absolute distance between depth observations and the predictions on a regression, and then taking the mean over all observations. MSE is the average of the squared difference between observations and predictions. RMSE is the square root of MSE and represents the standard deviation of residuals.

The classification accuracy of each model for six distinct depth classes was also evaluated, including 0–1 m, 1–2 m, 2–5 m, 5–10 m, 10–15 m, and 15–40 m classes. A confusion matrix was used for this, which permitted the calculation of overall accuracy, as well as individual producer's accuracy, user's accuracy, and F1-score metrics. Overall accuracy reflects the percentage of correctly classified pixels, user's accuracy reflects the misclassification error, producer's accuracy reflects the missing error, and F1 score is the harmonic mean of user's (i.e., precision) and producer's (i.e., recall) accuracy. These were calculated using the following:

$$OverallAccuracy = \frac{Number\ of\ correctly\ classified\ samples}{Total\ number\ of\ samples} \tag{7}$$

$$User's\ Accuracy = \frac{TP}{TP + FP} \tag{8}$$

$$Producer's\ Accuracy = \frac{TP}{TP + FN} \tag{9}$$

$$F1score = 2\left(\frac{User's\ acuracy \times Producer's\ accuracy}{User's\ acuracy + Producer's\ accuracy}\right) \tag{10}$$

where *TP* are true positives, *FP* are false positives, and *FN* are false negatives.

2.8. Model robustness evaluations

Here, robustness is defined as the preservation (i.e., stability) of a model's performance when exposed to erroneous inputs. Robustness was evaluated by exposing each model to changing gradients of training data set sizes (i.e., by reducing the size) and noise levels (i.e., by increasing noise within the training data). Similar systematic evaluations of ML model robustness have been performed in other studies (Caicedo et al., 2014).

Model robustness in the presence of multicollinearity was also evaluated. This phenomenon can be of concern because multicollinearity can weaken a model by reducing the precision of the estimated coefficients (Chan et al., 2022). Multicollinearity between input covariates was

tested for using two frequently applied indicators, tolerance (TOL) and Variable Inflation Factor (VIF):

$$TOL = 1 - R_{j}^2 \qquad (11)$$

$$VIF = \frac{1}{TOL}, \qquad (12)$$

where R_{j}^2 is the regression value of j on the other covariates in the data set. VIF measures how much the variance of a regression coefficient increases from collinearity. TOL is the reciprocal of VIF. It is generally agreed upon that a TOL value<0.01 and a VIF greater than 10 indicates the existence of multicollinearity (O'Brien, 2007). These thresholds were used to exclude variables from the modelling process.

2.9. Surface water extent classification

To identify surface water extent across the Upper Central Brooks Foothills region, the United States Geological Survey (USGS) high-resolution National Hydrography Dataset (NHD; https://nhd.usgs.gov/) was used. The NHD is a digital vector data set, representing the largest and most up-to-date database of waterbodies within the United States, and accordingly Alaska. To obtain a surface water extent classification, all lake and pond features from the NHD that intersected the study area were selected. All polygons were first reviewed (i.e., quality controlled) against optical basemap satellite imagery to ensure their accurate representation. Then, polygons were merged into one consistent layer, which was used as a processing mask for bathymetric modelling (Table 3).

3. Results

3.1. Spectral signatures by water depth

Optically derived spectral signatures for six bathymetric depth classes are presented in Fig. 4. There are visually discernable differences in the amount (%) of reflected radiation for each class, confirming the relationship between water depth and radiated energy passively measured by a satellite. With the shallower depth classes (e.g., up to 5 m), reflectance increases moving from the visible to infrared wavelengths, which suggests the presence of suspended materials (i.e., turbid conditions; Shi & Wang, 2014). In contrast, as depth increases (e.g., greater than 5 m), more energy becomes attenuated within the water column through absorption and scattering processes, which damp-

ens the measured reflectance, especially in the red edge and infrared regions. At these depths, spectral signatures are less distinct. For example, the deepest classes of 10–15 m and 15–40 m displayed some similarities in their spectral signatures, and even some overlap in the spectral range of 500–600 nm. Overall, differences in spectral reflectance were most apparent around ∼ 700–850 nm (i.e., the red edge and near infrared spectrums).

3.2. Model predictions

Regression evaluations for all models are presented in Fig. 5. Four metrics were used to assess the differences between model-derived bathymetry and field-derived depth. RF had the highest R^2 of 0.74, followed by SVR, CART, then MLR. RF also had the smallest MAE, MSE, and RMSE, with values of 2.12 m, 9.27 m, and 3.04 m, respectively. Similarly, SVR, CART, and MLR had progressively poorer performances. According to Fig. 5, all models demonstrated a general decrease in retrieval accuracy with water depth, especially MLR which could not reliably estimate depths beyond 10 m.

Confusion matrices were also used to assess model classification performance for six distinct depth classes. Classification results are presented in Tables 4 to 7. RF achieved the highest overall accuracy of 52.1%, followed by CART, SVR, and then MLR. RF also achieved the highest per-class F1 scores for four of the six depth classes. F1 scores ranged from 0.41 to 0.65 for RF, 0.31–0.61 for CART, 0.33–0.67 for SVR, and 0.0–0.57 for MLR.

3.3. Bathymetric mapping

Bathymetry was mapped for all waterbodies across the study region by applying the RF model within GEE, as this represented the most accurate algorithm assessed in this study. This process took 2.1 h to run within GEE. Bathymetric statistics were determined for 6282 waterbodies (Table 8). Fig. 6 shows bathymetric mapping examples produced by each model for five large Arctic lakes within the study area.

3.4. Model robustness

3.4.1. Sensitivity to training data size
The effect of training data size on model performance was evaluated by altering (i.e., reducing) the training set sizes in increments of 10%, and ranging from 10% (i.e., a

Table 3
Descriptive area statistics for waterbodies within the study area.

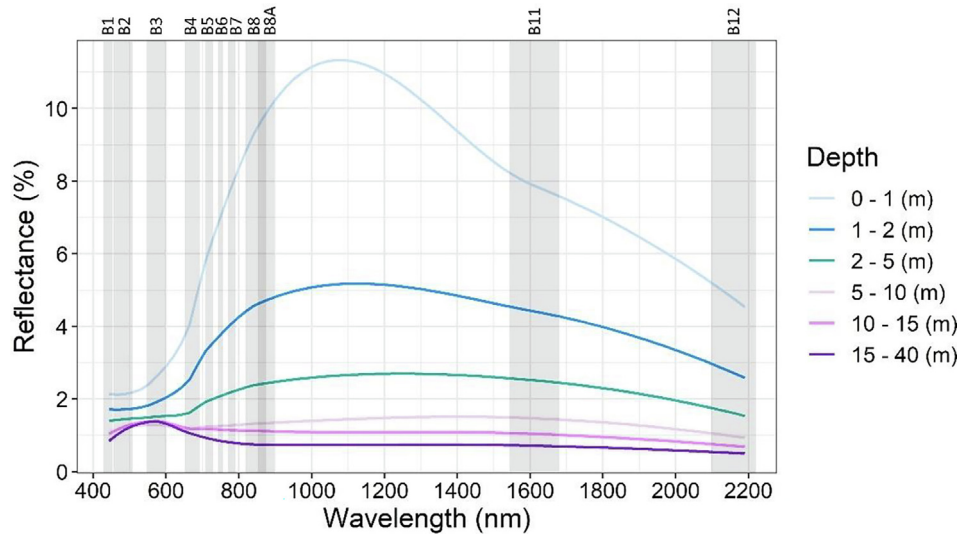| Type	Count	Waterbody Size (ha)					
		Minimum	**Maximum**	**Range**	**Std. Deviation**	**Mean**	**Median**
Lake/Pond	6282	5.6^{-4}	494.01	494.01	14.22	3.54	1.06

Fig. 4. Spectral signatures for six depth classes. Sentinel-2 bands and their band widths are also displayed in grey.
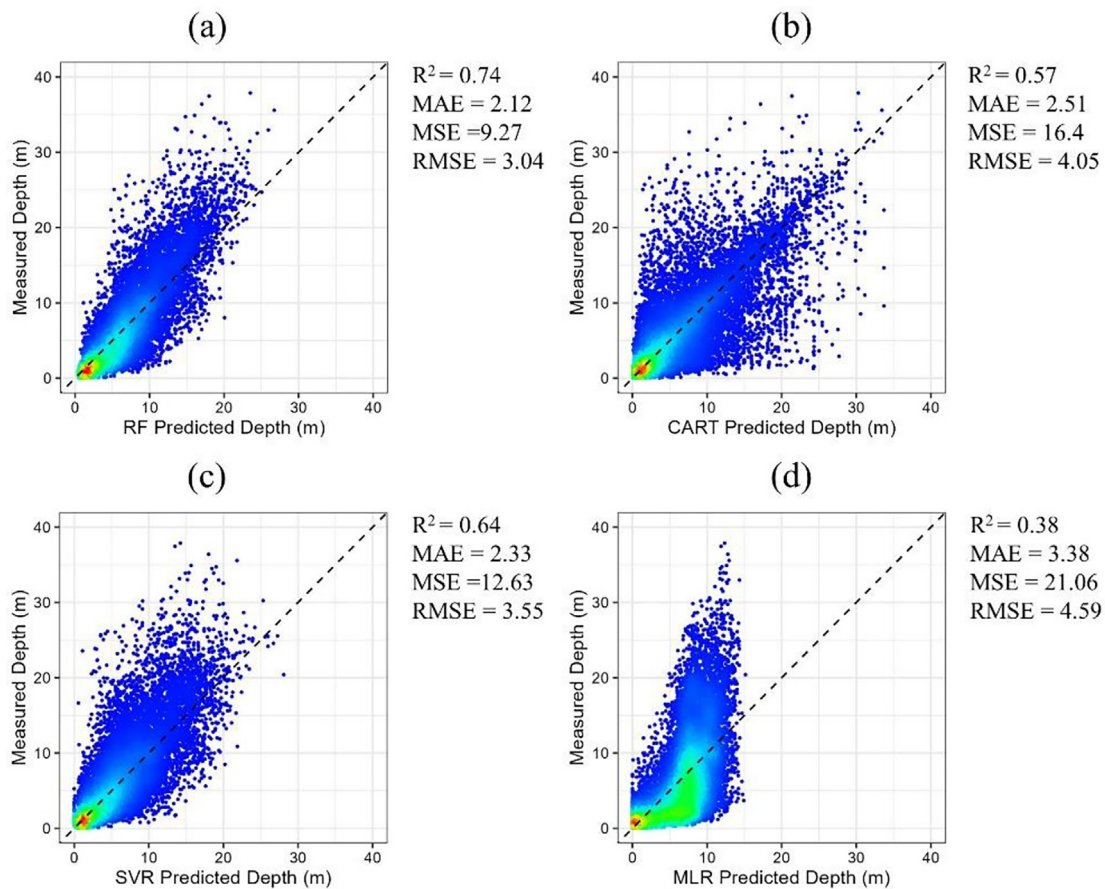

Fig. 5. Scatterplots of bathymetry predicted using each model versus in situ measured depth data. (a) RF. (b) CART. (c) SVR. (d) MLR.

very small sample size) to 100% (i.e., all samples were used; Table 9). Subsets of sample points were randomly selected from the training data for this assessment. Fig. 7 shows the sensitivity of each models' predictive performance (i.e., R^2) to declines in training set size. The non-parametric ML

algorithms, namely RF, SVR, and CART, were all negatively affected by reductions in training set size, whereas the parametric MLR showed a relatively stable, albeit very low performance. RF was the most accurate algorithm at all size reduction thresholds, although RF and SVR

Table 4
Confusion matrix for RF modelled bathymetry. Overall accuracy = 52.1%.

		Predicted Depth (m)						Producer's Accuracy (%)	F1 Score
		0–1	1–2	2–5	5–10	10–15	15–40		
In Situ Depth (m)	0–1	1150	388	103	7	0	0	69.8	0.65
	1–2	571	900	465	51	1	0	45.3	0.41
	2–5	179	1032	1989	761	56	13	49.4	0.51
	5–10	3	152	1237	2666	871	230	51.7	0.61
	10–15	0	2	47	343	728	759	38.7	0.41
	15–40	0	0	0	29	65	565	85.7	0.61
	User's Accuracy (%)	60.4	36.4	51.8	69.1	42.3	36.1		

Table 5
Confusion matrix for CART modelled bathymetry. Overall accuracy = 46.7%.

		Predicted Depth (m)						Producer's Accuracy (%)	F1 Score
		0–1	1–2	2–5	5–10	10–15	15–40		
In Situ Depth (m)	0–1	1150	388	103	7	0	0	45.9	0.59
	1–2	571	900	465	51	1	0	33.7	0.31
	2–5	179	1032	1989	761	56	13	45.1	0.44
	5–10	3	152	1237	2666	871	230	52.1	0.51
	10–15	0	2	47	343	728	759	41.2	0.42
	15–40	0	0	0	29	65	565	66.2	0.61
	User's Accuracy (%)	72.6	27.5	42.2	49.1	41.9	56.5		

Table 6
Confusion matrix for SVR modelled bathymetry. Overall accuracy = 47.3%.

		Predicted Depth (m)						Producer's Accuracy (%)	F1 Score
		0–1	1–2	2–5	5–10	10–15	15–40		
In Situ Depth (m)	0–1	1150	388	103	7	0	0	54.4	0.67
	1–2	571	900	465	51	1	0	41.1	0.36
	2–5	179	1032	1989	761	56	13	46.1	0.47
	5–10	3	152	1237	2666	871	230	48.2	0.51
	10–15	0	2	47	343	728	759	33.4	0.33
	15–40	0	0	0	29	65	565	75.6	0.53
	User's Accuracy (%)	79.5	30.4	48.8	54.3	33.1	29.8		

Table 7
Confusion matrix for MLR modelled bathymetry. Overall accuracy = 37.1%.

		Predicted Depth (m)						Producer's Accuracy (%)	F1 Score
		0–1	1–2	2–5	5–10	10–15	15–40		
In Situ Depth (m)	0–1	1150	388	103	7	0	0	57.1	0.57
	1–2	571	900	465	51	1	0	36.1	0.24
	2–5	179	1032	1989	761	56	13	36.4	0.31
	5–10	3	152	1237	2666	871	230	35.1	0.56
	10–15	0	2	47	343	728	759	25.7	0.24
	15–40	0	0	0	29	65	565	0.0	0.0
	User's Accuracy (%)	56.8	11.4	25.8	76.5	23.1	0.0		

Table 8
Descriptive statistics for the final bathymetric database of the study area. Statistics were derived from the RF model.

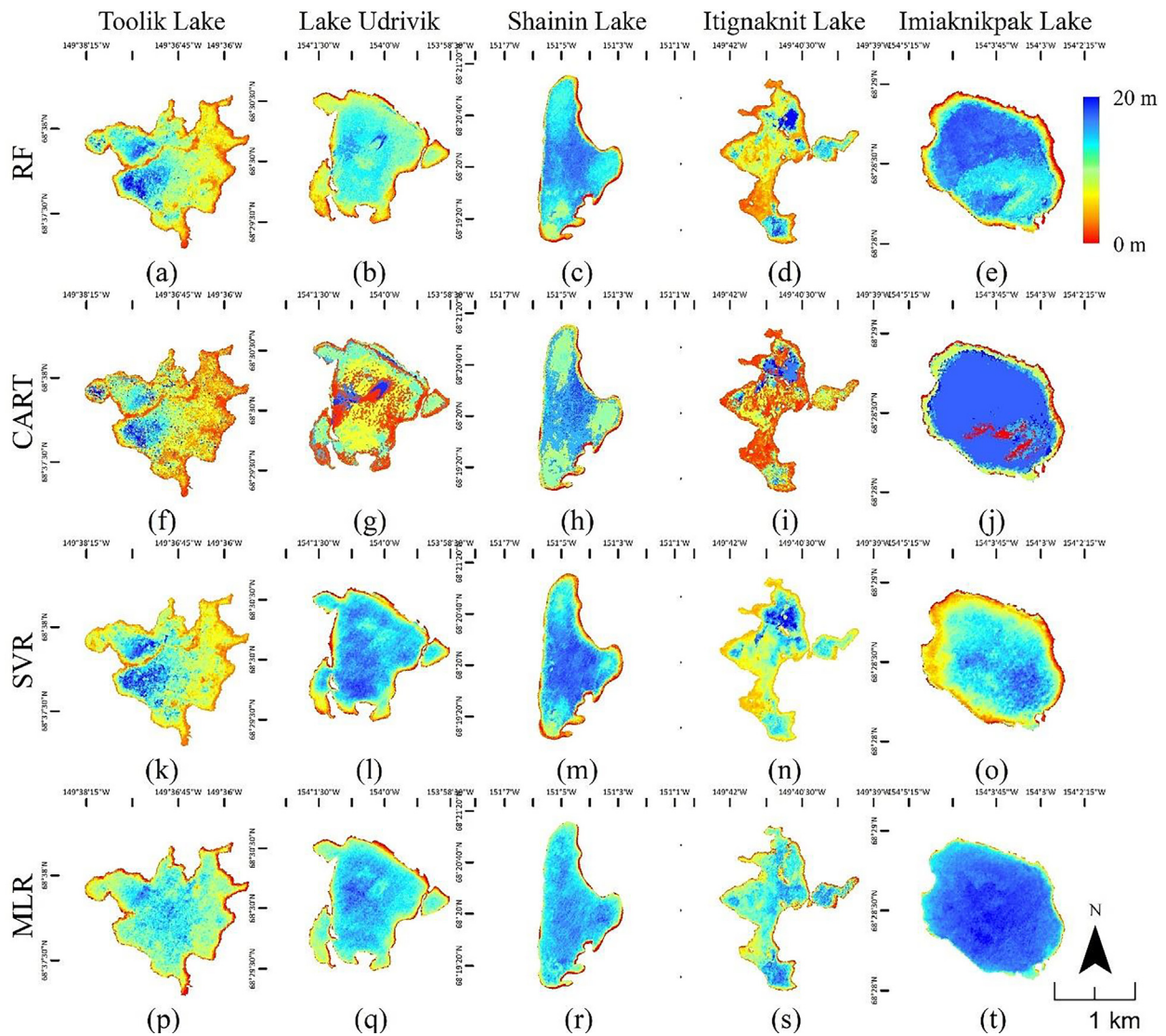| Number of Waterbodies	Lake Depth (m)					
	Minimum	Maximum	Range	Std. Deviation	Mean	Median
6282	0.25	27.05	26.80	1.51	2.42	2.02

Fig. 6. Bathymetry examples for five large lakes within the study area. (a-e) RF examples. (f-j) CART examples. (k-o) SVR examples. (p-t) MLR examples.

Table 9
Training data alterations used for examining the effect of size on model performance.

Training Set Size									
100%	90%	80%	70%	60%	50%	40%	30%	20%	10%
Samples Used for Model Training									
15,694	14,124	12,555	10,985	9416	7847	6277	4708	3138	1569

displayed comparable declines in accuracy and thus were similar in their stability. CART showed the greatest declines in predictive performance, particularly once the data set size was reduced to 50%.

3.4.2. Sensitivity to noise

The effect of noise on model performance was evaluated by randomly corrupting subsets of the training data (Zhu & Wu, 2004). To simulate noise, a random and normally distributed set of numerical values, which were based on the range (i.e., min and max) of the training data set, was first generated. Subsets of training samples, ranging from 10% of the data set to 100%, were then replaced with these noisy, incorrect values (Table 10). As seen in Fig. 8, the effect of noise was more pronounced on model performance than reductions in training data size. RF and SVR showed similar declines in performance, whereas CART had a sharp decline in R^2 with each successive threshold
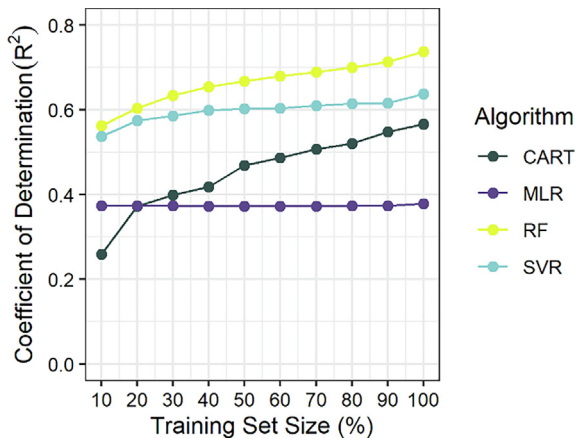
Fig. 7. Effects of training set size reduction on algorithm performance.

of noise inclusion. Nevertheless, RF was the most robust algorithm at eight out of 10 noise thresholds. MLR showed relatively high stability and low performance again, except at the 90% noise threshold, at which point a sharp decline in R^2 was seen.

3.4.3. Addressing multicollinearity

Satellite-based remote sensing technology allows for the collection of vast amounts of spectral data, and while this presents opportunities for enhanced environmental mapping and modelling, this can also cause data analysis issues such as multicollinearity (Chan et al., 2022). The results of the multicollinearity assessment based on TOL and VIF are presented in Table 11. These results suggest collinearity exists among the independent covariates. Thus, variables with a TOL value < 0.01 and a VIF greater than 10 were removed. Test evaluations of parsimonious models after removing these variables are presented in Fig. 9. All algorithms experienced a decline in performance after removing the potentially correlated variables. Loss in predictive accuracy was quite similar for each algorithm, although SVR did have the largest decline in R^2 from 0.64 to 0.41.

4. Discussion

In the current study, a ML-driven methodology was applied within GEE's web-based infrastructure to map bathymetry with Sentinel-2 data over the Alaskan tundra.

Three advanced ML algorithms, in addition to a conventional MLR algorithm, were comprehensively tested for their predictive capabilities and stability when exposed to erroneous data. Algorithms were quantitatively benchmarked by their accuracies, with results indicating that the RF ensemble ML algorithm performed best for estimating Arctic water depth. In contrast, MLR demonstrated the poorest performance, representing a R^2 difference of (-) 0.36 when compared to RF. This suggests that ML-driven algorithms may be more appropriate than simple regression models for bathymetric retrieval over inland Arctic environments, and especially where water depth and spectral reflectance lack linearity, such as in sediment-laden waters (Kamal & El-Ashmawy, 2023; Manessa et al., 2016). Evaluation of the scatterplot in Fig. 5a indicates that the best performing RF model could reliably retrieve depths close to 20 m. Much of the residual error associated with the RF model is concentrated around ± 5 m, and follows a normal distribution, as seen in Fig. 10. The spatial distribution of residuals associated with the RF model were also mapped over Toolik Lake (Fig. 11), since a large number of samples were collected there, and allowed for visual analysis of error characteristics. Overall, these results are consistent with previous studies that have shown RF to be the most reliable ML algorithm within GEE for a variety of regression (Aksoy et al., 2022; Hu et al., 2020; M. Zhang et al., 2021) and classification (Pan et al., 2022; Praticò et al., 2021) problems.

Results also demonstrated that RF was the most robust algorithm in the presence of artificial noise and modifications to training set size. For example, RF had the highest R^2 at almost all training reduction (10 out of 10) and noise corruption (eight out of 10) thresholds. This is an important finding because despite the immense number of studies on SDB, few of them have examined ML tolerance to noisy or partial data. Moreover, understanding the robustness property of ML models can help with generalization capabilities, and lessening overfitting (Xu et al., 2009). Measurements produced from real surveys often to some degree contain inaccuracies, which may cause poor predictive performance (Atla et al., 2011). This makes having knowledge of an algorithms capacity to tolerate different degrees of distorted data essential (Boateng et al., 2020). With this information, one can properly choose a ML algorithm for a given task.

Table 10
Training data alterations used for examining the effect of size on model performance.

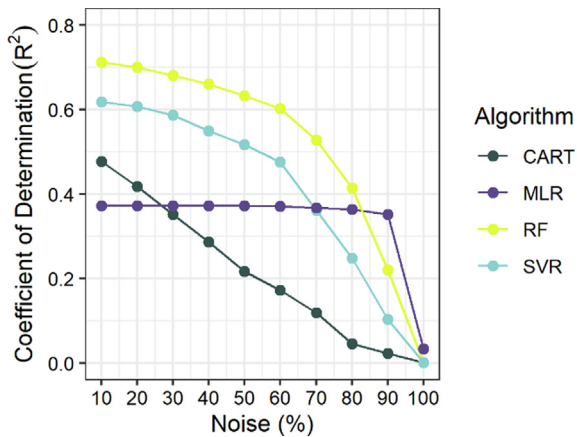| Noise Threshold									
100%	90%	80%	70%	60%	50%	40%	30%	20%	10%
Number of Corrupt Samples in the Training Data Set									
15,694	14,124	12,555	10,985	9416	7847	6277	4708	3138	1569

Fig. 8. Effects of noise on algorithm performance.

Table 11
Multicollinearity assessment results.

Variable	TOL	VIF
lnB1	0.423	2.364
lnB2	0.012	81.932
lnB3	0.008	120.254
lnB4	0.019	52.477
lnB5	0.017	58.256
lnB6	0.006	162.178
lnB7	0.005	193.416
lnB8	0.010	10.001
lnB8A	0.007	137.288
lnB11	0.009	100.643
lnB12	0.014	70.853
lnB2/lnB3	0.129	7.696
lnB2/lnB3	0.177	5.618
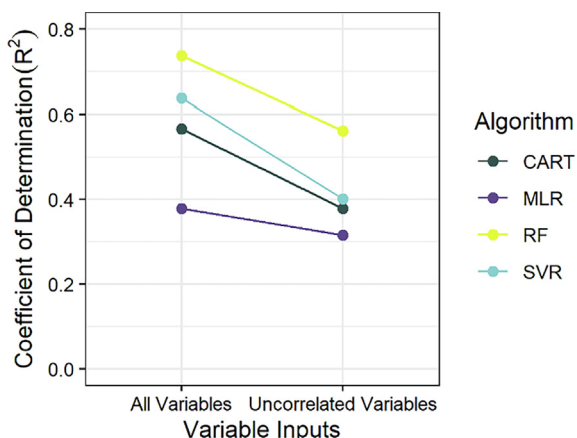
Fig. 9. Effects of removing correlated variables on algorithm performance.

Using TOL and VIF factors, the collinearity of log-transformed reflectance bands was evaluated which confirmed their high correlation. Variable selection was then applied by removing variables with potentially redundant information. In some cases, reducing dimensionality through correlation-based approaches can result in similar or even improved model performance (Cai et al., 2018; Georganos et al., 2018; Maxwell et al., 2018). However, the tests in this study demonstrated adverse losses in predictive accuracy when correlated variables were removed. This was the case for all algorithms, although RF consistently remained the most accurate. Similar to other studies, this finding suggests that using several optical bands increases the robustness of ML depth retrieval (Dekker et al., 2011; Lyzenga et al., 2006), even in the likely presence of multicollinearity. Nevertheless, an advantage of using a more parsimonious data set was the reduction in computational efforts (e.g., memory and time), which has implications for extending this work over even larger spatial extents within the GEE.

Lastly, it is imperative to discuss the apparent value of red to infrared bands in this study. As previously stated, many SDB studies recommend that shorter wavelengths with the lowest level of light absorption are optimal for bathymetric applications (Ashphaq et al., 2021). However, in the present study, wavelengths from 665 nm and beyond also displayed noticeably distinct spectral responses at depths < 5 m (Fig. 4), in addition to relatively high correlations (-0.58 to −0.65; Table 2) to in situ survey measurements. In a recent study over the Arctic Coastal Plain (ACP) of Alaska, Simpson et al. (2021) found the Landsat-8 red band (654 nm) useful for bathymetric modelling in the presence of turbidity. This is because suspended sediment impedes the penetration of blue and green light into the water column, while increasing reflectance for longer wavelengths. This provides explanation to the present study, as many lakes in the Toolik region are considered turbid from glacial flour contributions and impacts of riparian soil from melting of banks (Sierszen et al., 2003). For example, observed through secchi depth measurements, Toolik Lake has shallow light penetration (e.g., 2 to 4 m) due to high levels of dissolved humic organic matter (O'Brien et al., 1997). Hence the increase in water leaving radiation measured over shallow depths in Fig. 4. Collectively, Arctic lakes and ponds span a wide range of bottom-reflectance conditions and optical properties of the water column (Rautio et al., 2011), necessitating the employment of multi-band imagery with measurements beyond the visible spectrum. Chen et al. (2022), for example, measured the correlation between Landsat-8 bands and Alaskan lake depths and found the red and shortwave infrared bands to be slightly more correlated than the blue, green, and coastal bands, although all correlations were weak ranging from −0.11 to −0.20. While not conducted over the Arctic, there are other studies demonstrating the high sensitivity of red and/or infrared light emitted from multispectral sensors to water depths, particularly in shallow depths (∼2 m) or in turbid conditions (George, 1997; Manessa et al., 2016; Muzirafuti et al., 2020; Roberts & Anderson, 1999).
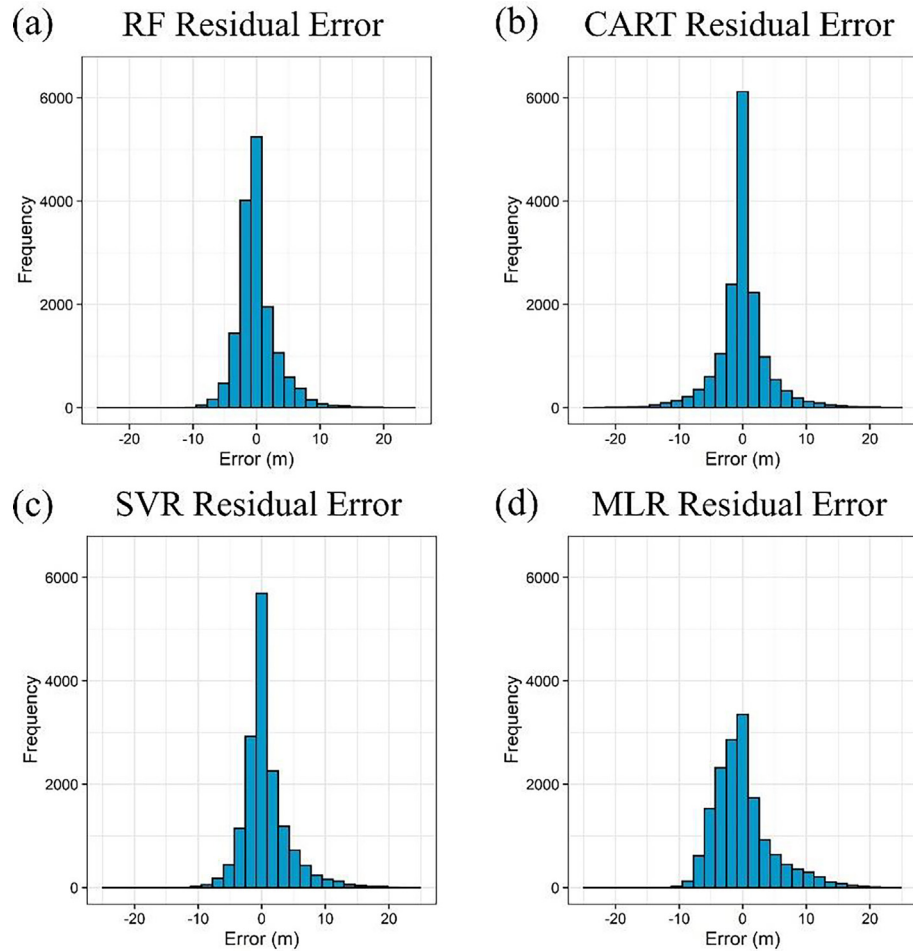
Fig. 10. Histograms of residual errors, calculated as the difference between in situ measured water depth and model predicted water depth. (a) RF. (b) CART. (c) SVR. (d) MLR.
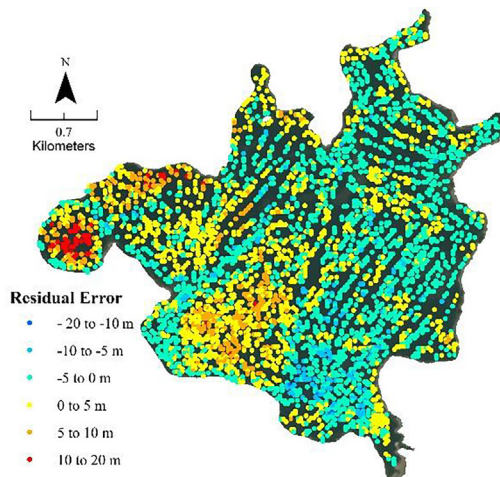

Fig. 11. Spatial distribution map of residual error values from the best performing RF model, over Toolik Lake, with optical imagery underneath.

5. Conclusions

Lakes and ponds constitute a large fraction of the circumpolar region, especially in the Arctic permafrost lowlands. Timely and accurate products that characterize the physical properties of these important freshwater systems are needed, especially due to escalating pressures from global climate warming. However, the Arctic is a vast region that is sparsely inhabited, making conventional survey-based mapping a costly and difficult endeavor. This challenge was addressed in this study by developing a cloud-based methodology within the GEE platform that predicts Arctic water depth using ML and remote sensing technologies. By leveraging GEE for data processing and modelling, this methodology can be applied rapidly, efficiently, and over large spatial extents of the Arctic. Additionally, this was one of the first studies to employ Sentinel-2 satellite imagery over inland Arctic regions for modelling bathymetry. Thus, the resulting water depth maps are of high resolution (e.g., 10 m), and cost-effective due to the open-source nature of the ESA's Sentinel-2 satellites.

Through a comprehensive examination, the efficacy and robustness of several ML algorithms available within the GEE cloud-based platform was also established, and compared to a conventional regression modelling method (e.g., MLR). Results showed that RF is the most suitable

algorithm for the task of inland Arctic bathymetric retrieval. Compared to SVR, CART, and MLR, this algorithm was able to predict bathymetry more accurately, especially when subjected to unideal conditions (e.g., noise, training data alterations, and multicollinearity).

It is expected that this scalable ML methodology will contribute to large-scale bathymetric mapping updates over inland Arctic tundra regions. Such data is essential for flood risk assessments, river maintenance, habitat mapping, and numerous conservation initiatives, to name a few.

Declaration of Competing Interest

The authors declare that they have no known competing financial interests or personal relationships that could have appeared to influence the work reported in this paper.

Acknowledgements

References

Ahola, R., Chénier, R., Horner, B., Faucher, M.-A., & Sagram, M. (2018). Satellite derived bathymetry for Arctic charting: a review of sensors and techniques for operational implementation within the Canadian Hydrographic Service. *Proc. SPIE 10784, Remote Sensing of the Ocean,Sea Ice, Coastal Waters, and Large Water Regions*, 1078407.

Aksoy, S., Yildirim, A., Gorji, T., Hamzehpour, N., Tanik, A., Sertel, E., 2022. Assessing the performance of machine learning algorithms for soil salinity mapping in Google Earth Engine platform using Sentinel-2A and Landsat-8 OLI data. Adv. Space Res. 69, 1072–1086.

Amani, M., Ghorbanian, A., Ahmadi, S.A., Kakooei, M., Moghimi, A., Mirmazloumi, S.M., Moghaddam, S.H.A., Mahdavi, S., Ghahremanloo, M., Parsian, S., Wu, Q., Brisco, B., 2020. Google Earth Engine cloud computing platform for remote sensing big data applications: A comprehensive review. IEEE J. Sel. Top. Appl. Earth Obs. Remote Sens. 13, 5326–5350.

Ashphaq, M., Srivastava, P. K., & Mitra, D. (2021). Review of near-shore satellite derived bathymetry: Classification and account of five decades of coastal bathymetry research. In *Journal of Ocean Engineering and Science* (Vol. 6, pp. 340–359). Shanghai Jiaotong University.

Ashphaq, M., Srivastava, P.K., Mitra, D., 2022. Analysis of univariate linear, robust-linear, and non-linear machine learning algorithms for satellite-derived bathymetry in complex coastal terrain. Reg. Stud. Mar. Sci. 56. https://doi.org/10.1016/j.rsma.2022.102678 102678.

Atla, A., Tada, R., Sheng, V., Singireddy, N., 2011. Sensitivity of different machine learning algorithms to noise. J. Comput. Sci. Colleges 26 (5), 96–103 https://www.researchgate.net/publication/234825892.

Boateng, E.Y., Otoo, J., Abaye, D.A., 2020. Basic tenets of classification algorithms K-nearest-neighbor, support vector machine, random forest and neural network: A review. J. Data Anal. Inform. Process. 8, 341–357.

Breiman, L., 2001. Random forests. Mach. Learn. 45, 5–32.

Bring, A., Fedorova, I., Dibike, Y., Hinzman, L., Mård, J., Mernild, S.H., Prowse, T., Semenova, O., Stuefer, S.L., Woo, M.K., 2016. Arctic terrestrial hydrology: A synthesis of processes, regional effects, and research challenges. J. Geophys. Res. G: Biogeosci. 121, 621–649.

Bukata, R., Jerome, J., Kondratyev, K., Pozdnyakov, D., 2018. Optical properties and remote sensing of inland and coastal waters. CRC Press.

Caballero, I., Stumpf, R.P., 2019. Retrieval of nearshore bathymetry from Sentinel-2A and 2B satellites in South Florida coastal waters. Estuar. Coast. Shelf Sci. 226 106277.

Cai, J., Luo, J., Wang, S., Yang, S., 2018. Feature selection in machine learning: a new perspective. Neurocomputing, 70–79 http://www.elsevier.com/open-access/userlicense/1.0/.

Caicedo, J.P.R., Verrelst, J., Munoz-Mari, J., Moreno, J., Camps-Valls, G., 2014. Toward a semiautomatic machine learning retrieval of biophysical parameters. IEEE J. Sel. Top. Appl. Earth Obs. Remote Sens. 7 (4), 1249–1259.

Campbell, J., Wynne, R., 2011. Introduction to remote sensing. Guilford Press.

Carroll, M.L., Loboda, T.V., 2017. Multi-decadal surface water dynamics in North American tundra. Remote Sens. (Basel) 9 (497), 1–15.

Casal, G., Monteys, X., Hedley, J., Harris, P., Cahalane, C., McCarthy, T., 2019. Assessment of empirical algorithms for bathymetry extraction using Sentinel-2 data. Int. J. Remote Sens. 40 (8), 2855–2879.

Chan, J., Leow, S. M. H., Bea, K. T., Cheng, W. K., Phoong, S. W., Hong, Z. W., & Chen, Y. L. (2022). Mitigating the Multicollinearity Problem and Its Machine Learning Approach: A Review. In *Mathematics* (Vol. 10, Issue 1283, pp. 1–17). MDPI.

Chen, H., Yunus, A.P., Nukapothula, S., Avtar, R., 2022. Modelling Arctic coastal plain lake depths using machine learning and Google Earth Engine. Phys. Chem. Earth 126 103138.

Chénier, R., Faucher, M.A., Ahola, R., 2018. Satellite-derived bathymetry for improving Canadian Hydrographic Service charts. ISPRS Int. J. Geo Inf. 7 (306), 1–15.

Cooley, S., Smith, L., Ryan, J., Pitcher, L., Pavelsky, T., 2019. Arctic-Boreal Lake Dynamics Revealed Using CubeSat Imagery. Geophys. Res. Lett. 46 (4), 2111–2120.

Dekker, A.G., Phinn, S.R., Anstee, J., Bissett, P., Brando, V.E., Casey, B., Fearns, P., Hedley, J., Klonowski, W., Lee, Z.P., Lynch, M., Lyons, M., Mobley, C., Roelfsema, C., 2011. Intercomparison of shallow water bathymetry, hydro-optics, and benthos mapping techniques in Australian and Caribbean coastal environments. Limnol. Oceanogr. Methods 9, 396–425.

Dickens, K., Armstrong, A., 2019. Application of machine learning in satellite derived bathymetry and coastline detection. SMU Data Sci. Rev. 2 (1), 4 https://scholar.smu.edu/datasciencereviewAvailableat: https://scholar.smu.edu/datasciencereview/vol2/iss1/4http://digital-repository.smu.edu.

Ellis, J.M., Calkin, P.E., 1979. Nature and Distribution of Glaciers, Neoglacial Moraines, and Rock Glaciers, East-Central Brooks Range, Alaska. Arctic Alpine Res. 11 (4), 403–420 https://www.tandfonline.com/action/journalInformation?journalCode=uaar20.

Eugenio, F., Marcello, J., Mederos-Barrera, A., Marques, F., 2022. High-resolution satellite bathymetry mapping: Regression and machine learning-based approaches. IEEE Trans. Geosci. Remote Sens. 60, 5407614.

Gafoor, F., Al-Shehhi, M.R., Cho, C.S., Ghedira, H., 2022. Gradient boosting and linear regression for estimating coastal bathymetry based on Sentinel-2 images. Remote Sens. (Basel) 14 (5037), 1–18.

Gao, J., 2009. Bathymetric mapping by means of remote sensing: Methods, accuracy and limitations. Prog. Phys. Geogr. 33 (1), 103–116.

Gautam, A., & Singh, V. (2020). Parametric versus non-parametric time series forecasting methods: A review. In *Journal of Engineering Science and Technology Review* (Vol. 13, Issue 3, pp. 165–171). Eastern Macedonia and Thrace Institute of Technology.

Georganos, S., Grippa, T., Vanhuysse, S., Lennert, M., Shimoni, M., Kalogirou, S., Wolff, E., 2018. Less is more: optimizing classification performance through feature selection in a very-high-resolution remote sensing object-based urban application. GIScience Remote Sens. 55 (2), 221–242.

George, D.G., 1997. Cover Bathymetric mapping using a Compact Airborne Spectrographic Imager (CASI). Int. J. Remote Sens. 18 (10), 2067–2071.

Gorelick, N., Hancher, M., Dixon, M., Ilyushchenko, S., Thau, D., Moore, R., 2017. Google Earth Engine: Planetary-scale geospatial analysis for everyone. Remote Sens. Environ. 202, 18–27.

Guohe, F., 2011. Parameter optimizing for support vector machines classification. Comput. Eng. Appl. 47, 123–124.

Hassan, H.M., Nadaoka, K., 2017. Assessment of machine learning approaches for bathymetry mapping in shallow water environments using multispectral satellite images. Article Int. J. Geoinform. 13 (2), 1–15 https://www.researchgate.net/publication/318066655.

Hedley, J.D., Roelfsema, C., Brando, V., Giardino, C., Kutser, T., Phinn, S., Mumby, P.J., Barrilero, O., Laporte, J., Koetz, B., 2018. Coral reef applications of Sentinel-2: Coverage, characteristics, bathymetry and benthic mapping with comparison to Landsat 8. Remote Sens. Environ. 216, 598–614.

Hinkel, K., Sheng, Y., Lenters, J.D., Lyons, E.A., Beck, R.A., Eisner, W. R., Wang, J., 2012. Thermokarst Lakes on the Arctic Coastal Plain of Alaska: Geomorphic Controls on Bathymetry. Permafr. Periglac. Process. 23, 218–230.

Hopkins, D., 1949. Thaw Lakes and Thaw Sinks in the Imuruk Lake Area, Seward Peninsula, Alaska. J. Geol. 57 (2), 119–131 https://www. jstor.org/stable/30063635?seq=1&cid=pdf-.

Hu, Y., Xu, X., Wu, F., Sun, Z., Xia, H., Meng, Q., Huang, W., Zhou, H., Gao, J., Li, W., Peng, D., Xiao, X., 2020. Estimating forest stock volume in Hunan Province, China, by integrating in situ plot data, Sentinel-2 images, and linear and machine learning regression models. Remote Sens. (Basel) 12 (186), 1–23.

Ibori, C.O., Knudby, A., 2020. An approach to minimize atmospheric correction error and improve physics-based satellite-derived bathymetry in a coastal environment. Remote Sens. (Basel) 12 (2752), 1–22.

Jepsen, S.M., Voss, C.I., Walvoord, M.A., Minsley, B.J., Rover, J., 2013. Linkages between lake shrinkage/expansion and sublacustrine permafrost distribution determined from remote sensing of interior Alaska, USA. Geophys. Res. Lett. 40, 882–887.

Kamal, N., El-Ashmawy, N., 2023. Potential of Using Machine Learning Regression Techniques to Utilize Sentinel Images for Bathymetry Mapping of Nile River, Egypt. J. Remote Sens. Space Sci. 26 (3), 545–555 https://linkinghub.elsevier.com/retrieve/pii/S1110982323000431.

Lawrence, R., Wright, A., 2001. Rule-based classification systems using classification and regression tree (CART) analysis. Photogramm. Eng. Remote Sens. 67 (10), 1137–1142.

Legleiter, C.J., Roberts, D.A., 2005. Effects of channel morphology and sensor spatial resolution on image-derived depth estimates. Remote Sens. Environ. 95, 231–247.

Legleiter, C.J., Tedesco, M., Smith, L.C., Behar, A.E., Overstreet, B.T., 2014. Mapping the bathymetry of supraglacial lakes and streams on the Greenland ice sheet using field measurements and high-resolution satellite images. Cryosphere 8, 215–228.

Li, J., Knapp, D.E., Lyons, M., Roelfsema, C., Phinn, S., Schill, S.R., Asner, G.P., 2021. Automated global shallowwater bathymetry mapping using google earth engine. Remote Sens. (Basel) 13 (1469), 1–17.

Liu, Y., Islam, A., Gao, J., 2003. Quantification of shallow water quality parameters by means of remote sensing. Prog. Phys. Geogr. 27 (1), 24–43.

Louis, J., Debaecker, V., Pflug, B., Main-Knorn, M., Bieniarz, J., Mueller-Wilm, U., Cadau, E., Gascon, F., 2016. Sentinel-2 Sen2Cor: L2A processor for users. Living Planet Sympos.

Lyzenga, D., 1978. Passive remote sensing techniques for mapping water depth and bottom features. Appl. Opt. 17 (3), 379–383.

Lyzenga, D., Malinas, N., Tanis, F., 2006. Multispectral bathymetry using a simple physically based algorithm. IEEE Trans. Geosci. Remote Sens. 44 (8), 2251–2259.

Manabe, S., Stouffer, R., 1980. Sensitivity of a global climate model to an increase of CO2 concentration in the atmosphere. J. Geophys. Res. 85 (C10), 5529–5554.

Manessa, M.D.M., Kanno, A., Sekine, M., Haidar, M., Yamamoto, K., Imai, T., Higuchi, T., 2016. Satellite derived bathymetry using random forest algorithm and worldview-2 imagery. Geoplan.: J. Geomat. Plan. 3 (2), 117.

Manessa, M., Kanno, A., Sekine, M., Haidar, M., Yamamoto, K., Imai, T., Higuchi, T., 2016. Satellite-derived bathymetry using random forest algorithm and worldview-2 imagery. Geoplan.: J. Geomat. Plan. 3 (2), 117–126.

Maulud, D., Abdulazeez, A.M., 2020. A review on linear regression comprehensive in machine learning. J. Appl. Sci. Technol. Trends 1 (4), 140–147.

Maxwell, A.E., Warner, T.A., Fang, F., 2018. Implementation of machine-learning classification in remote sensing: An applied review. Int. J. Remote Sens. 39 (9), 2784–2817.

Mishra, D.R., Narumalani, S., Rundquist, D., Lawson, M., 2005. Characterizing the vertical diffuse attenuation coefficient for down-welling irradiance in coastal waters: Implications for water penetration by high resolution satellite data. ISPRS J. Photogramm. Remote Sens. 60, 48–64.

Misra, A., Vojinovic, Z., Ramakrishnan, B., Luijendijk, A., Ranasinghe, R., 2018. Shallow water bathymetry mapping using Support Vector Machine (SVM) technique and multispectral imagery. Int. J. Remote Sens. 39 (13), 4431–4450.

Mountrakis, G., Im, J., Ogole, C., 2011. Support vector machines in remote sensing: A review. ISPRS J. Photogramm. Remote Sens. 66, 247–259.

Mudiyanselage, S.S.J.D., Abd-Elrahman, A., Wilkinson, B., Lecours, V., 2022. Satellite-derived bathymetry using machine learning and optimal Sentinel-2 imagery in South-West Florida coastal waters. GIScience Remote Sens. 59 (1), 1143–1158.

Muhammad, F., Sidiq, T., Sakti, A., Windupranata, W., Adytia, D., & Poerbandono. (2020). Bathymetric Modeling from Time Series of Multispectral Satellite Images by Using Google Earth Engine: Understanding Error Distribution by Depth. *International Conference on Data Science and Its Applications*.

Muller, S., Walker, D., & Jorgenson, M. (2018). *Land Cover and Ecosystem Map Collection for Northern Alaska*. ORNL DAAC.

Muster, S., Heim, B., Abnizova, A., Boike, J., 2013. Water body distributions across scales: A remote sensing based comparison of three arctic tundra wetlands. Remote Sens. (Basel) 5, 1498–1523.

Muzirafuti, A., Barreca, G., Crupi, A., Faina, G., Paltrinieri, D., Lanza, S., Randazzo, G., 2020. The contribution of multispectral satellite image to shallowwater bathymetry mapping on the Coast of Misano Adriatico, Italy. J. Marine Sci. Eng. 8 (126), 1–21.

Niroumand-Jadidi, M., Vitti, A., Lyzenga, D., 2018. Multiple Optimal Depth Predictors Analysis (MODPA) for river bathymetry: Findings from spectroradiometry, simulations, and satellite imagery. Remote Sens. Environ. 218, 132–147.

O'Brien, R.M., 2007. A caution regarding rules of thumb for variance inflation factors. Qual. Quant. 41, 673–690.

O'Brien, W., Bahr, M., Hershey, A., Hobbie, J., Kipphut, G., Kling, G., Kling, H., McDonald, M., Miller, M., Rublee, P., Vestal, R., 1997. The limnology of Toolik Lake. In: Freshwaters of Alaska. Springer, pp. 61–106.

Paltan, H., Dash, J., Edwards, M., 2015. A refined mapping of Arctic lakes using Landsat imagery. Int. J. Remote Sens. 36 (23), 5970–5982.

Pan, X., Wang, Z., Gao, Y., Dang, X., Han, Y., 2022. Detailed and automated classification of land use/land cover using machine learning algorithms in Google Earth Engine. Geocarto Int. 37 (18), 5415–5432.

Pe'eri, S., Madore, B., Nyberg, J., Snyder, L., Parrish, C., & Smith, S. (2016). Identifying bathymetric differences over alaska's north slope

using a satellite-derived bathymetry multi-temporal approach. *Journal of Coastal Research*, *76*(sp1), 56–63.

Pérez-Cutillas, P., Pérez-Navarro, A., Conesa-García, C., Zema, D.A., Amado-Álvarez, J.P., 2023. What is going on within google earth engine? A systematic review and meta-analysis. Remote Sens. Appl.: Soc. Environ. 29 100907.

Plevris, V., Solorzano, G., Bakas, N., & Ben Seghier, M. (2022). Investigation of Performance Metrics in Regression Analysis and Machine Learning-Based Prediction Models. *World Congress in Computational Mechanics and ECCOMAS Congress.*

Plug, L.J., West, J.J., 2009. Thaw lake expansion in a two-dimensional coupled model of heat transfer, thaw subsidence, and mass movement. J. Geophys. Res. Earth 114, F01002.

Polcyn, F., Brown, W., & Sattinger, I. (1970). *The Measurement of Water Depth by Remote Sensing Techniques.*

Poursanidis, D., Traganos, D., Reinartz, P., Chrysoulakis, N., 2019. On the use of Sentinel-2 for coastal habitat mapping and satellite-derived bathymetry estimation using downscaled coastal aerosol band. Int. J. Appl. Earth Obs. Geoinf. 80, 58–70.

Praticò, S., Solano, F., di Fazio, S., Modica, G., 2021. Machine learning classification of mediterranean forest habitats in google earth engine based on seasonal sentinel-2 time-series and input image composition optimisation. Remote Sens. (Basel) 13 (586), 1–28.

Rautio, M., Dufresne, F., Laurion, I., Bonilla, S., Vincent, W.F., Christoffersen, K.S., 2011. Shallow freshwater ecosystems of the circumpolar Arctic. Ecosci. 18 (3), 204–222.

Richards, S., Leighton, T., 2003. High frequency sonar performance predictions for littoral operations-the effects of suspended sediments and micro-bubbles. J. Defence Sci. 8 (1), 1–7.

Riordan, B., Verbyla, D., McGuire, A.D., 2006. Shrinking ponds in subarctic Alaska based on 1950–2002 remotely sensed images. J. Geophys. Res. Biogeo. 111, G04002.

Roberts, A.C.B., Anderson, J.M., 1999. Shallow water bathymetry using integrated airborne multi-spectral remote sensing. Int. J. Remote Sens. 20 (3), 497–510.

Sagawa, T., Yamashita, Y., Okumura, T., Yamanokuchi, T., 2019. Satellite derived bathymetry using machine learning and multi-temporal satellite images. Remote Sens. (Basel) 11 (1155), 1–19.

Saylam, K., Brown, R., Hupp, J., 2017. Assessment of depth and turbidity with airborne Lidar bathymetry and multiband satellite imagery in shallow water bodies of the Alaskan North Slope. Int. J. Appl. Earth Obs. Geoinf. 58, 191–200.

Selimovic, V., Ketcherside, D., Chaliyakunnel, S., Wielgasz, C., Permar, W., Angot, H., Millet, D.B., Fried, A., Helmig, D., Hu, L., 2022. Atmospheric biogenic volatile organic compounds in the Alaskan Arctic tundra: constraints from measurements at Toolik Field Station. Atmos. Chem. Phys. 22, 14037–14058.

Shah, A., Deshmukh, B., Sinha, L.K., 2020. A review of approaches for water depth estimation with multispectral data. World Water Policy, 6. John Wiley and Sons Inc., pp. 152–167.

Shi, W., Wang, M., 2014. Ocean reflectance spectra at the red, near-infrared, and shortwave infrared from highly turbid waters: A study in the Bohai Sea, Yellow Sea, and East China Sea. Limnol. Oceanogr. 59 (2), 427–444.

Sierszen, M.E., Mcdonald, M.E., Jensen, D.A., 2003. Benthos as the basis for arctic lake food webs. Aquat. Ecol. 37, 437–445.

Simpson, C.E., Arp, C.D., Sheng, Y., Carroll, M.L., Jones, B.M., Smith, L.C., 2021. Landsat-derived bathymetry of lakes on the Arctic Coastal Plain of northern Alaska. Earth Syst. Sci. Data 13, 1135–1150.

Stuckey, J., Noguera, J., Bogardus, R., & McPherson, R. (2019). Bathymetric data from Lower Campsite Lake, Toolik Field Station, Alaska (2015). *Arctic Data Center.*

Stumpf, R.P., Holderied, K., Sinclair, M., 2003. Determination of water depth with high-resolution satellite imagery over variable bottom types. Limnology and Oceanography 48, 547–556.

Sui, Y., Fu, D., Wang, X., Su, F., 2018. Surface water dynamics in the North America arctic based on 2000–2016 Landsat Data. Water 10 (824), 1–12.

Surisetty, V.V.A.K., Venkateswarlu, C., Gireesh, B., Prasad, K.V.S.R., Sharma, R., 2021. On improved nearshore bathymetry estimates from satellites using ensemble and machine learning approaches. Adv. Space Res. 68, 3342–3364.

Tonion, F., Pirotti, F., Faina, G., Paltrinieri, D., 2020. A machine learning approach to multispectral satellite derived bathymetry. ISPRS Ann. Photogramm. Remote Sens. Spatial Inform. Sci. 5 (3), 565–570.

Traganos, D., Poursanidis, D., Aggarwal, B., Chrysoulakis, N., Reinartz, P., 2018. Estimating satellite-derived bathymetry (SDB) with the Google Earth Engine and sentinel-2. Remote Sens. (Basel) 10 (859), 1–18.

Verrelst, J., Camps-Valls, G., Muñoz-Marí, J., Rivera, J., Veroustraete, F., Clevers, J., & Moreno, J. (2015). Optical remote sensing and the retrieval of terrestrial vegetation bio-geophysical properties - A review. In *ISPRS Journal of Photogrammetry and Remote Sensing* (Vol. 108, pp. 273–290). Elsevier B.V.

Vincent, W., Laurion, I., Pienitz, R., & Anthony, K. (2013). Climate impacts on Arctic lake ecosystems. In *Climatic Change and Global Warming of Inland Waters : Impacts and Mitigation for Ecosystems and Societies* (Vol. 27).

Walker, D., Reynolds, M., Daniëls, F., Einarsson, E., Elvebakk, A., Gould, W., Katenin, A., Kholod, S., Markon, C., Melnikov, E., Moskalenko, N., Talbot, S., Yurtsev, B., 2005. The circumpolar Arctic vegetation map. J. Veg. Sci. 16, 267–282.

Xu, H., Caramanis, C., Mannor, S., 2009. Robustness and regularization of support vector machines. J. Mach. Learn. Res. 10, 1485–1510.

Yang, H., Guo, H., Dai, W., Nie, B., Qiao, B., Zhu, L., 2022. Bathymetric mapping and estimation of water storage in a shallow lake using a remote sensing inversion method based on machine learning. Int. J. Digital Earth 15 (1), 789–812.

Yunus, A.P., Dou, J., Song, X., Avtar, R., 2019. Improved bathymetric mapping of coastal and lake environments using sentinel-2 and landsat-8 images. Sensors 19, 1–20.

Zhang, J.Y., Zhang, J., Ma, Y., Chen, A.N., Cheng, J., Wan, J.X., 2019. Satellite-derived bathymetry model in the arctic waters based on support vector regression. J. Coast. Res. 90 (sp1), 294–301.

Zhang, M., Zhang, M., Yang, H., Jin, Y., Zhang, X., Liu, H., 2021. Mapping regional soil organic matter based on sentinel-2a and modis imagery using machine learning algorithms and google earth engine. Remote Sens. (Basel) 13 (2934), 1–21.

Zhu, X., Wu, X., 2004. Class noise vs. attribute noise: A quantitative study. Artif. Intell. Rev. 22, 177–210.